Microscopically informed upscale approach of modelling damage in mortar by considering matrix-to-grain interface and grain micro-fracture characteristics

Abderrahmane Rhardane, Syed Yasir Alam, Frédéric Grondin

Microscopically informed upscale approach of modelling damage in mortar by considering matrix-to-grain interface and grain micro-fracture characteristics

Abderrahmane RHARDANE, Syed Yasir ALAM, Frédéric GRONDIN*

Institut de Recherche en Génie Civil et Mécanique (GeM), UMR 6183, Centrale Nantes – Université de Nantes - CNRS, 1 rue de la Noë 44321 Nantes, France

abderrahmane.rhardane@ec-nantes.fr
syed-yasir.alam@ec-nantes.fr
frederic.grondin@ec-nantes.fr (corresponding author)

Abstract

Multiscale modelling of damage in cement-based materials is mostly done through a downscale approach and constitutive laws are developed based on quasi-brittleness or cracking process within these materials. However, the microscopic characteristics of each phase in these materials need to be considered in order to accurately predict the durability. This article presents an experimentally-validated multiscale approach to model damage in mortar which takes into account the microscale fracture properties of the cement paste, the grain and the interface in-between them. This numerical study, on the one hand, shows that the failure is significantly dependent on the interface properties between cement paste and sand grains, which should be modelled as a separate phase with different properties than the bulk matrix. On the other hand, this study reveals that sand grain failure and grain size effect are the key phenomena to consider for the precise prediction of damage in the cement-based materials.

Keywords: micromechanics; grain size effect; mortar; interface, failure; multiscale modelling.

1. Introduction

Mesoscale simulations are more and more used to represent the heterogeneous nature in micromechanical modelling for concrete [1]–[6]. In cementitious materials like concrete or mortar, the heterogeneous material structure ranges from nanometres to millimetres of length scale. In mesoscale modelling, the mesostructure is often represented as a three-phase system consisting of randomly placed granular inclusions embedded inside a homogenous binding cement paste matrix and an interfacial transition zone (ITZ) between aggregates and the matrix. Subsequently, the cement paste is generally modelled as a homogenous material because the representation of its heterogeneous nature requires downscaling to the micrometric and sub-micrometric scales and is not the object of much attention compared to the concrete. However, damage and durability loss in cementitious materials is often associated with the local properties of the cement paste. In multiscale numerical modelling of cementitious composites, the properties of the different phases are conventionally calibrated through inverse analysis using downscale approach e.g. the properties of cement paste, ITZ and sand grains are calibrated through experiments at the concrete scale.

While this downscale approach has been successfully used [7]–[13], it raises few questions regarding its robustness. In fact, the calibration of the model parameters of each phase requires extensive experimental tests that can be burdensome and time-consuming. Moreover, calibration and experiments have to be repeated every time the mix-design changes. On top of that, lack of any assessment of the properties found at lower scales renders the approach less robust. Fichant et al. [14] proposed a continuum-based damage model for concrete with parameters linked to the experimentally measured properties. However, these parameters need to be calibrated using experimental results, and require recalibration when the concrete composition is no longer the same.

A calibration-free mesoscopic modelling of damage in cement-based materials calls for a microscopically-informed approach; i.e. one that takes into account (i) the complex aspects of the hardening or hydration process in cement paste microstructure; (ii) the matrix-grain interface properties which is not the same as of the bulk matrix; and (iii) grain properties, their particle size distribution and their physical fracture mechanisms. Once determined, these subscale properties can be validated with experimental measurements to as low as the nanoscale [15]–[18]. Eventually, the upscale approach can be applied without resorting to repetitive calibrations at the upper scales. Bernard et al. [8] proposed an upscale approach using properties of cement paste that are determined using numerical simulations at the microscale. However, due to limitations of the model and the lack of properties regarding cement paste's phases, the softening curve of the mortar was not correctly reproduced. Sherzer et al. [5] proposed another upscale modelling method using the Lattice Discrete Particle Model [6] to determine the properties of the cement paste matrix from the microscale. While, the macroscopic behaviour of concrete is correctly reproduced, it is done so by calibrating model parameters.

The main goal of this paper is to present an upscale approach for multiscale damage modelling in mortar specimens that is free of parameter recalibration at the microscale. Also, a discussion is proposed regarding the influence of the properties of ITZ and the inclusions' micro-fracture on the global behaviour of cementitious materials. The cement paste’s properties are first determined at the microscopic scale using a hydration model and applying intrinsic properties of hydration products, and then experimentally validated in order to render a calibration-free approach. The properties of hydration products remain the same in case of change in the hydration age or in the mix-design. At the mesoscale, a newly developed random particle generation algorithm is applied to create the mesostructure, which is composed of sand particles, cement paste and ITZ. Full particle size distribution curve of sand

is considered. Properties of sand particles not only consist of the elastic properties and failure strength but the physical failure mechanisms due to their grain size effect. ITZ properties are determined by considering the boundary effect on the hydration process and the porosity. Multiscale approach is outlined and the constitutive damage behaviour is presented. Three-point-bending tests on mortar specimens are simulated and the influencing parameters, particularly the ITZ properties and the grain size effect, are discussed in detail. A parametric study is conducted with the aim of identifying the influence of the fracture properties of the ITZ.

2. Damage mesoscale modelling in cementitious materials

2.1 Bridging length scales: from cement paste to mortar

A concrete mesostructure (with a scale range from 10^{-3} to 10^{-1}m) can be thought of as a three-phase material that is composed of coarse aggregates embedded in a mortar matrix with an ITZ, as shown in Figure 1. The mortar matrix (with a scale range from 10^{-4} to 10^{-3}m) can itself be decomposed further into sand particles, an ITZ and a binding cement paste matrix. The bulk cement paste matrix (with a scale range from 10^{-6} to 10^{-4}m) is a heterogeneous composite made of unhydrated particles (issued from clinker) ingrained in a matrix of different hydrates. To simulate the damage of these materials at each scale, a mesostructure is generated and then converted into a finite element mesh. A damage law is attributed to such phases, using parameters that are linked to either physical properties or upscaled homogenised properties.

The principles of the upscaling approach can be summarised as:

- The mix composition is defined (i.e. type of cement, particle size distribution of clinker and additives, mix proportions, w/c ratio, curing conditions, volume fractions of fine and coarse aggregates, etc.).
- The representative elementary volume (REV) of the virtual microstructure of cement paste is generated through a hydration model. The hydration platform Virtual Cement and Concrete Testing Laboratory, or VCCTL [19], is used in this case and converted into a finite element mesh. Simulation of the hydration processes does not require any calibration.
- The damage law developed by Fichant et al. [14], [20] is used for damage modelling for all cement phases. A full description of the model and its application to cementitious materials is given in Matallah et al. [21].
- The parameters of the micromechanical damage model for each cement paste phase (elastic moduli, tensile strength and fracture energy) are linked to the physical properties of the respective phase. These parameters are considered intrinsic to the model, and can be used for any cement paste composition.
- Uniaxial tension and compression simulations of the cement paste's REV are conducted to obtain the macroscopic stress-strain response and fracture properties.
- The VCCTL hydration model is used once again to simulate the hydration of cement paste near a fixed boundary. This exemplifies the evolution of cement hydration in the ITZ near the fine aggregates of mortar. Its properties are calculated using analytical homogenisation methods.
- At the scale of mortar, the mesostructure is generated via the newly developed zone-of-influence random particle generation method and converted into a FE mesh in the finite element code Cast3M.
- Damage model is attributed to each phase of the mortar. The regularisation of the damage model follows the energetic approach proposed by Matallah et al. [21] and

the REV length h is taken as 200µm, which the thickness of the finite element chosen for the mesoscopic simulations. This length also corresponds to the size of the cement paste's Representative Elementary Volume (REV) at the microscale. The mechanical properties are already known either at the microscale (cement paste and ITZ) or from physical properties and failure mechanisms (sand).

- Simulation of damage in mortar at the mesoscale is launched. Stress-strain response, failure properties and cracking characteristics can be obtained.
- In order to proceed to the level of concrete, tensile and compressive tests can be simulated in order to determine the stress-strain curve of mortar, which can be used to determine the properties of the mortar matrix at the scale of concrete.

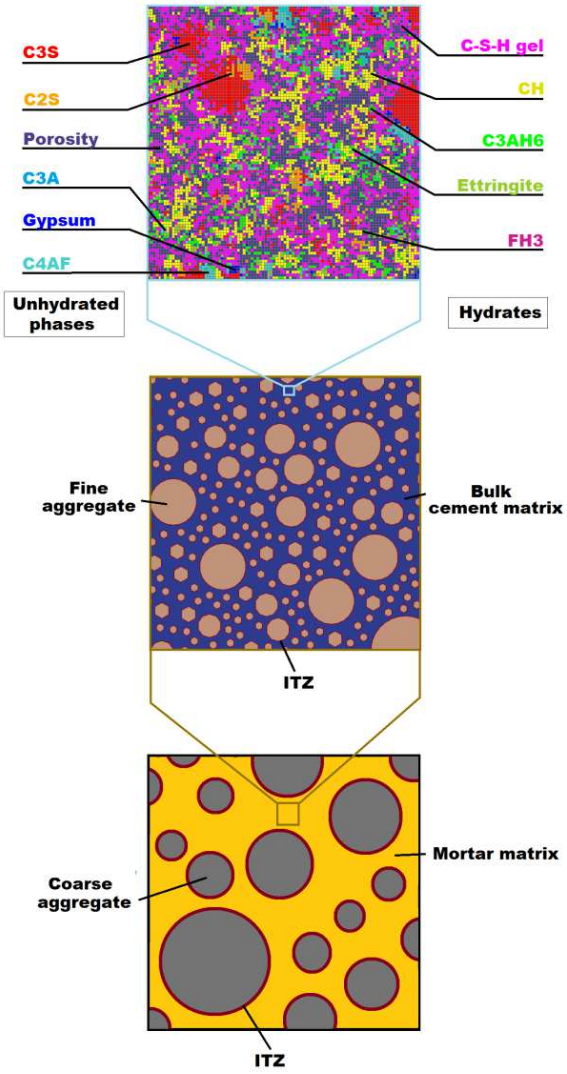

Figure 1. *Schematization of the multiscale modelling of concrete mesostructure.*

A damage model [14], [20] is applied to all the phases with model parameters, namely Young's modulus E, Poisson's ratio ν, tensile strength f_t and fracture energy G_f, varying from phase to phase. In damage mechanics, the total stress $\boldsymbol{\sigma}$ is calculated from the effective stress $\tilde{\boldsymbol{\sigma}}$ using a damage tensor. In the isotropic form of the damage model mentioned above, the relationship can be written as:

$$\boldsymbol{\sigma} = (1-D_T)\left\{\tilde{\boldsymbol{\sigma}}\right\}_+ + (1-D_C)\left\{\tilde{\boldsymbol{\sigma}}\right\}_- \quad (1)$$

where D_T and D_C are respectively the isotropic damage variables in tension and in compression. It is assumed that damage grows only due to the tensile opening mode, with the equivalent strain calculated using:

$$\varepsilon_{eq} = \sqrt{\sum \{\varepsilon_{ii}\}_+^2} \tag{2}$$

where $\{\bullet\}$ are the Macaulay brackets. Given the following damage evolution law:

$$D_T = 1 - \frac{\kappa_0}{\varepsilon_{eq}} \exp\left[-B_T\left(\varepsilon_{eq} - \kappa_0\right)\right] \tag{3}$$

the damage is linked to the phase properties (E, v, f_t and G_f), that is:

$$\kappa_0 = \frac{f_t}{E} \tag{4}$$

$$B_T = f_t\left(\frac{G_f}{h} - \frac{f_t^2}{2E}\right)^{-1} \tag{5}$$

This study is limited to the scale of mortar. However, it can be easily extended to concrete. The composition studied is made of a 0-4 mm size rolled river sand (44.7% of the mortar volume) and a type I Portland cement with a w/c ratio of 0.45. Three notched beams of 7×7×28 cm in size are tested under three-point bending at the age of 28 days, and the Force - Crack Mouth Opening Displacement (F-CMOD) curve is used to compare the experimental measurements with the numerical results. The mix-design is given in Table 1 and the experimental F-CMOD curve is shown in Figure 2.

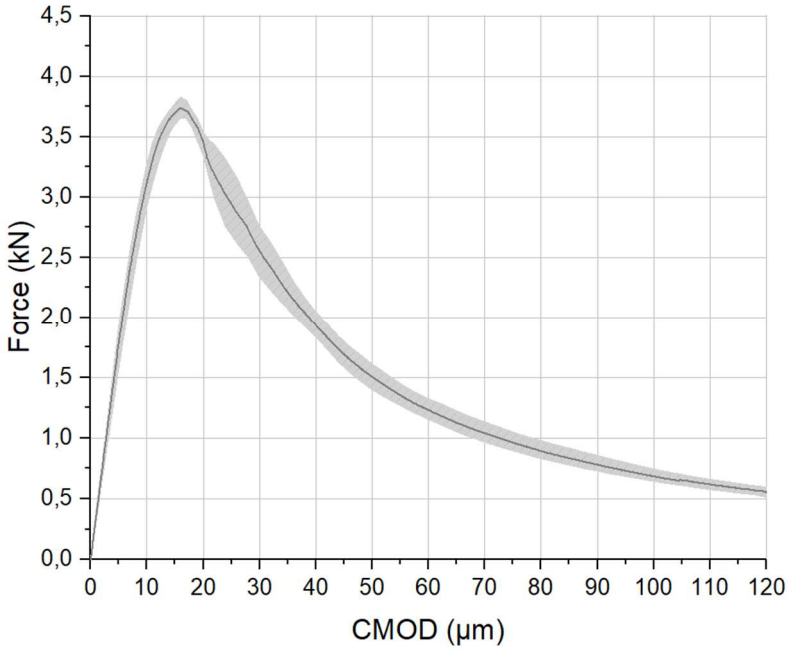

Figure 2. *Experimental F-CMOD curve of mortar (thick line represents average behaviour over three beams).*

Table 1. *Mix design of the studied mortar.*

	Sand	*CEM I 52.5 N*	*Effective water*	*Added water*
Mass (kg/m^3)	1175	668	300	305
Density	2.63	3.12	1	1

2.2. Microscale properties of cement paste

In cementitious materials, cement paste is considered as the matrix that binds the aggregate particles. It is composed of hydration products formed by hydration reaction between cement materials and water, as well as unhydrated cement particles and residual water. Cement paste can be represented at two scales: the molecular scale (with a scale range from 10^{-8} to 10^{-6} m) and the microscopic scale (with a scale range from 10^{-6} to 10^{-4} m) [22]–[26]. The former can be used to determine the intrinsic properties of the components (i.e. hydration products) independently of the type of cement, the hydration degree or the water-to-cement (w/c) ratio. The microscopic scale considers an assembly of the components based on their volumetric proportions for a given hydration degree, mix ratio and cement type. If the intrinsic properties of cement paste components are known, any assembly can be generated and modelled. The cement paste assembly should be defined by a REV which should be small enough to consider all components explicitly, and big enough to represent the building element at the upper scale (laboratory sample). Various sizes for the REV are proposed in the literature which vary from merely 50 µm up to 400 µm [10], [27]–[31]. This variation is explained by the fact that the REV size depends on the heterogeneities, e.g. clinker particles, which decrease in size with hydration. A parametric analysis is carried out by simulating tensile tests on multiple microstructures varying with REV size, and plotting the average tensile strength, the standard deviation, and the coefficient of variation, as shown in Figure 3. It is observed that the coefficient of variation falls below 5% when choosing a size of 200 µm. This size is therefore best suited for damage computations of mature cement pastes. The choice of this REV size satisfies the condition that it must be at least three to five times the size of the biggest inclusion [32].

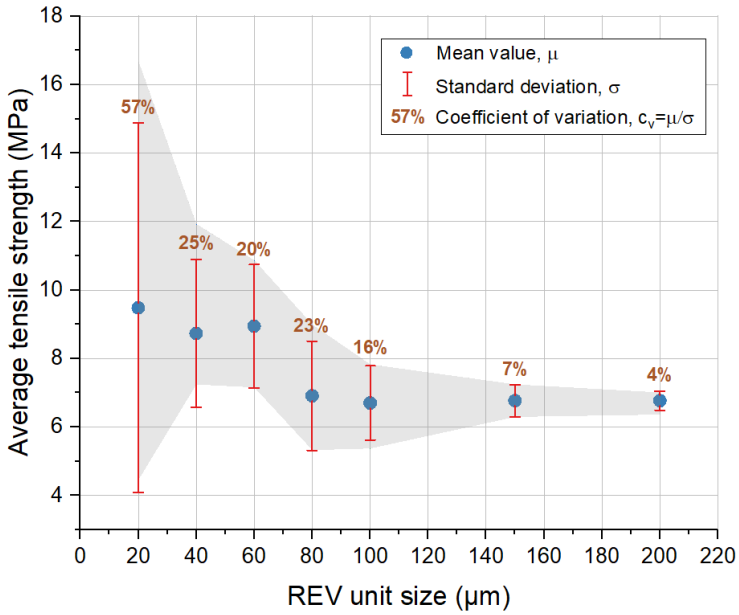

Figure 3. *influence of the REV size on the results of damage computation.*

The microstructure of the cement paste was obtained by the hydration software VCCTL [33] and a mesh algorithm [34] was used to import the virtual microstructure in the finite element code Cast3M [35]. The input parameters include the cement composition (C_3S=72.2%, C_2S=9.4%, C_3A= 9.4%, C_4AF=7.8%, $K\bar{S}$=1.3%, $N\bar{S}$=0.3%), the added gypsum (4.2%), the particle size distribution of cement (obtained by laser diffraction), the w/c ratio (0.45), the curing conditions (20°C, isothermal and sealed) and the cycle-time conversion curve (calculated from the isothermal calorimetry curve). All the input data are the characteristics of the cement and the mix design and do not require any calibration. The microstructure at 28 days is extracted and converted into a FE mesh. Cement phases are explicitly represented inside the microstructure, including calcium-silicate-hydrates (C-S-H) and the capillary porosity. The C-S-H gel is considered as a single homogenised component representing both low density C-S-H, high density C-S-H and gel porosity [36]. Water-filled porosity is also considered as another "component" regardless of the water content in the capillary voids. The resolution of the REV (the size of a voxel) is 1µm^3 and the volume of the REV is 200×200×200 µm^3. The obtained 3D microstructure is shown in Figure 4.

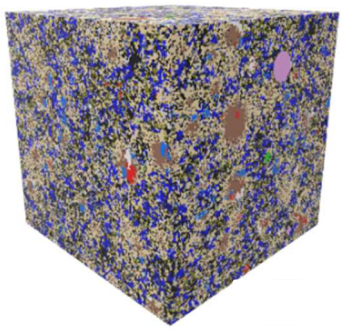

Figure 4. *3D virtual cement paste obtained by the VCCTL hydration platform*

Uniaxial tensile tests were simulated on cement pastes in order to obtain the homogenised mechanical properties. In the numerical calculation, each step considers a volume with new properties (issue from the last step) and small displacements were considered. So, 2D simulations can be used instead of 3D simulations which were too slow due to the huge number of voxels (equal to 8 million). 2D sections were extracted and simulations were conducted on them. The macroscopic results were averaged over four sections (labelled S50, S100, S150 and S200, as illustrated in Figure 5.

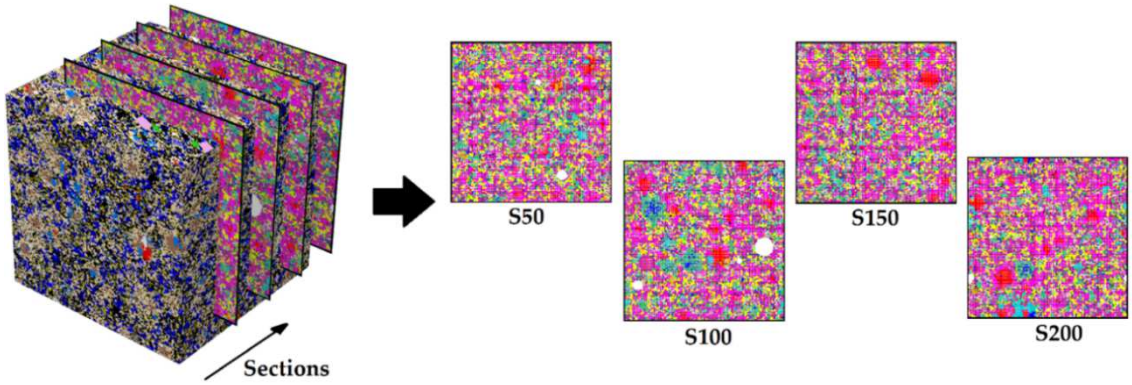

Figure 5. *Extraction of sections S50, S100, S150 and S200 from the 3D microstructure (colour code: purple = porosity, red = $\boldsymbol{C_3S}$, orange = $\boldsymbol{C_2S}$, blue = $\boldsymbol{C_3A}$, light blue = $\boldsymbol{C_4AF}$, dark blue = sulphate phases, white = inert particles, yellow = portlandite, pink = C-S-H, green = hydrogarnet and AFm, light green = ettringite).*

If the properties of the cement paste's phases are known, the multiscale approach of modelling damage can be carried out without any calibration, since the micromechanical model can be used for different cement paste compositions and mix designs. The elastic properties used in the model for each cement phase are obtained from the literature (see [37] for example). On the other hand, very little literature work can be found on the tensile strength and the fracture energy of individual cement phases. It is not practically possible to determine these fracture parameters for all cement phases. In previous studies [29], [38], the tensile strength was assumed to be proportional to the elastic modulus. However, an inverse analysis scheme is proposed instead to identify the missing properties used to calculate the model parameters. For this reason, the following assumptions are made [39], [40]:

i. Each voxel in the finite element mesh corresponds to a unique homogeneous phase,
ii. All voxels of the same type have the same mechanical properties,
iii. The behaviour of the cement paste's phases is considered isotropic,
iv. All phases obey the damage model presented above,
v. The tensile strength $f_{t,ph}$ is proportional to the micro-hardness, HD_{ph}, of the phase, i.e.

$$HD_{ph} = \alpha_{ft} \times f_{t,ph} \tag{6}$$

vi. The fracture energy $G_{f,ph}$ of each component is proportional to its elastic energy i.e.

$$G_{f,ph} = \beta_{Gf} \frac{(1+\nu) f_t^2}{E} \tag{7}$$

where α_{ft} and β_{Gf} are two proportionality constants. The first three assumptions reduce the number of elastic properties needed for the simulations, while the other two reduce the number of missing parameters that need to be identified. A relationship between the tensile strength and the hardness is generally attested for ductile metals, with $\alpha_{ft} = 3$, while the value of this coefficient varies from ~28 to 200 for composites, granular materials and ceramics [41]. The problem is therefore reduced to the only two unknown parameters (α_{ft} and β_{Gf}). To identify them, a reference cement paste has been used to carry out multiple tests, such as bending tests on notched specimens (40×40×160 mm^3), compressive tests on cement paste cubes (40×40×40 mm^3) and impulse excitation tests on unnotched beams [42]. This allows for the determination of the macroscopic properties of the reference cement paste, i.e. E_{HCP}, ν_{HCP}, $f_{t,HCP}$ and $G_{f,HCP}$. The use of an optimisation algorithm, such as the Levenberg-Marquardt method [43], for an inverse analysis is time consuming and cannot guarantee the uniqueness of the solution. For this reason, an alternative method based DOE, or the design of experiments method, is chosen. In this case, the parameters α_{ft} and β_{Gf} are fixed in a realistic range, $[15;\ 35]$ and $[1.25 \times 10^{-5};\ 6.25 \times 10^{-5}]$, respectively. Numerically, the cement paste composition is introduced in the hydration model and the virtual microstructure generated is used to perform simulations to determine the numerical properties of the cement paste (Figure 6). The average stress-crack opening displacement curve is calculated from the behaviour of all the four 2D sections for the values of α_{ft} and β_{Gf}, in order to determine the corresponding $f_{t,HCP}$ and $G_{f,HCP}$. The cement paste properties $f_{t,HCP}$ and $G_{f,HCP}$ are then drawn as a function of α_{ft} and β_{Gf}, as illustrated in Figure 7. In the same figure, the isopleths are drawn, and the

intersection of the contour lines that correspond to the experimental values for $f_{t,HCP}$ and $G_{f,HCP}$ show a unique solution for α_{ft} and β_{Gf}.

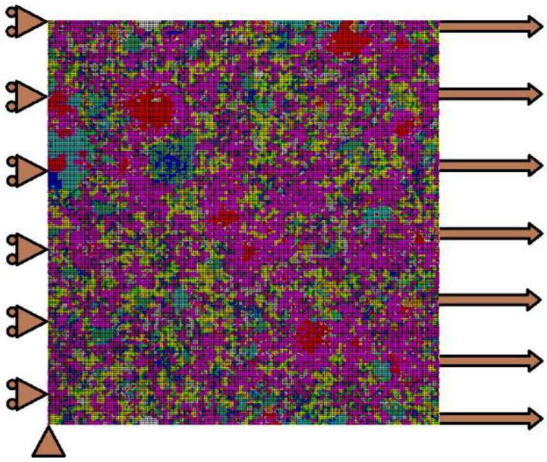

Figure 6. *Microstructure of cement paste under tensile loading.*

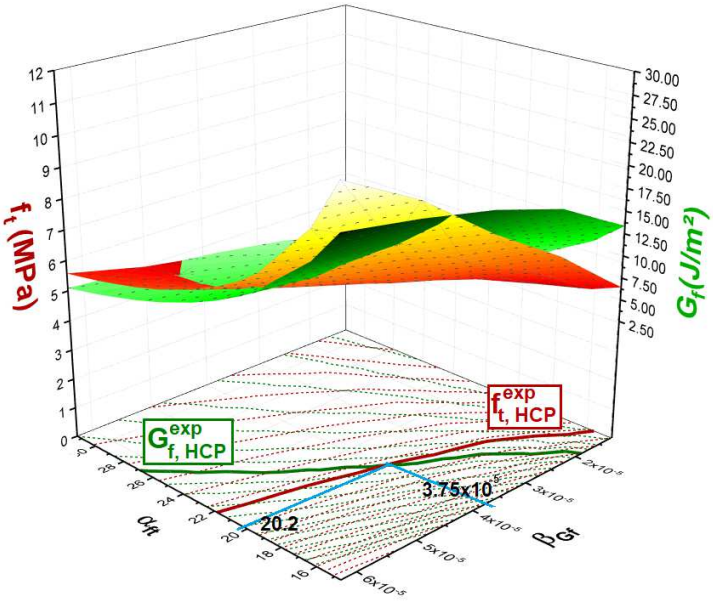

Figure 7. *Identification of the parameters* $\boldsymbol{\alpha_{ft}}$ *and* $\boldsymbol{\beta_{Gf}}$ *using experimental results.*

Once the parameters (α_{ft} and β_{Gf}) are determined, the fracture properties of each phase of the cement paste remain the same when the mix design changes, and are treated as intrinsic material properties [40]. The properties of the main phases of cement paste are listed in Table 2. Using these properties, it is possible to use the same procedure to estimate the mechanical properties of other cement pastes. Figure 8 shows a comparison between the estimated values and the experimental data, and demonstrate the potential of the micromechanical model to predict properties of cement pastes.

Figure 9 shows the results for the cement paste used in this article . It also shows a comparison between the simulation curve and the idealised behaviour of an isolated finite element of cement paste at the mortar scale with the same mechanical properties. The macroscopic properties of the hardened cement paste (HCP) are obtained: E_{HCP} = 16 GPa, ν_{HCP} = 0.27, $f_{t,HCP}$ = 6.77 MPa and $G_{f,HCP}$ = 6.81 J/m².

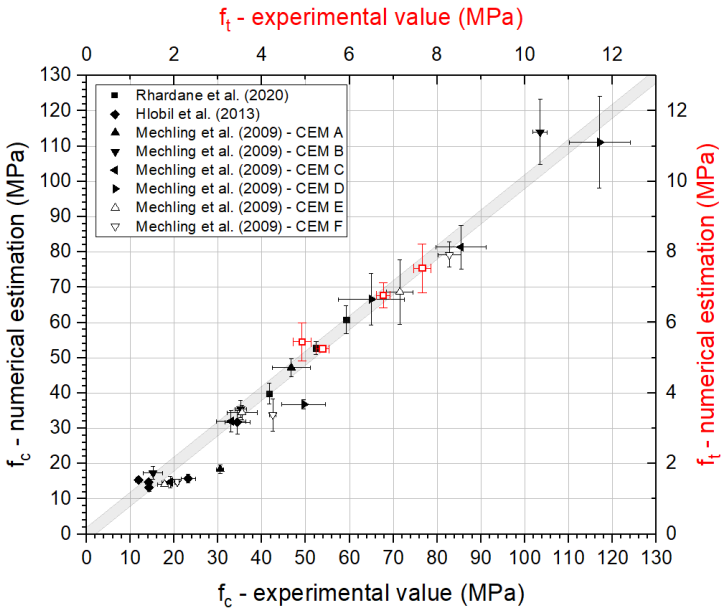

Figure 8. *Comparison of numerical results against experimental data for the compressive and tensile strength of different mix designs (the bars represent 1 S.D.).*

Table 2. *Properties of the main cement paste phases.*

Phase	E_{ph} *(GPa)*	ν_{ph} *(-)*	Refs.	HD_{ph} *(GPa)*	Refs.	$f_{t,ph}$ *(MPa)*	$G_{f,ph}$ *(J/m²)*
C_3S	137.4	0.30	[15], [28], [44]–[46]	8.7	[15], [46]	430.7	65.8
C_2S	135.5	0.30	[15], [28], [44]–[46]	8.0	[15]	396.0	56.3
C_3A	145.2	0.28	[15], [28], [44]–[46]	10.8	[15]	534.6	94.3
C_4AF	150.8	0.32	[15], [28], [44]–[46]	9.5	[15]	470.3	72.5
Gypsum	44.5	0.33	[28], [44], [45]	0.6	[47]	29.6	0.98
CH	43.5	0.29	[28], [44], [45]	1.5	[17], [48]	73.8	6.1
C-S-H	23.8	0.24	[49]–[51]	1.1	[17], [52]	55.0	5.9
Ettringite	24.1	0.32	[28], [44], [45]	0.8	[47], [53]	39.6	3.2
AFm	43.2	0.29	[28], [44]	5.3	[25]	262.4	77.3

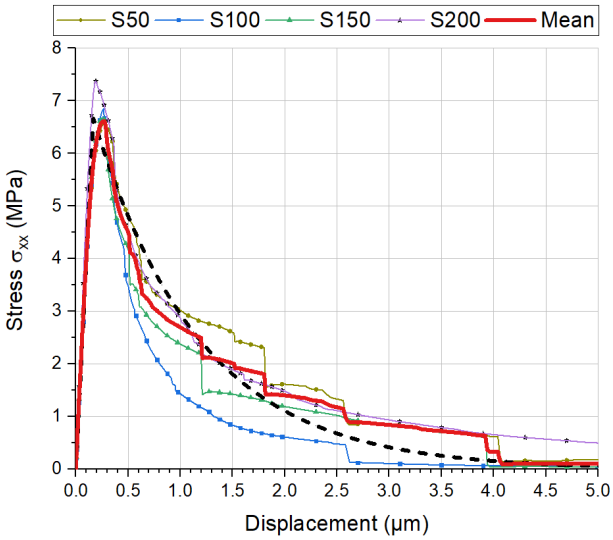

Figure 9. *The stress-crack opening displacement curve of the cement paste microstructure (CEM I, w/c = 0.45) using intrinsic micromechanical parameters (dashed line = idealised behaviour of a finite element representing cement paste at the scale of mortar).*

2.3. Interaction between the hardening cement paste and the rigid heterogeneities at mortar scale

In cementitious materials, it is generally accepted that the interface between rigid inclusions (sand or aggregate particles) and binding matrix (cement paste) is more porous and possesses different effective properties than the cement paste itself [54]. This interface has been classically modelled as a homogeneous layer that envelops the inclusions and several studies have used this approach to determine the homogenised elastic properties of the mortar mesostructure [55], [56]. This approach was not considered by [2], [57], [58], who proposed heterogeneous models by which the elastic properties evolve in the interface according to a power law. Similarly, [59] proposed a model of the interface consisting of several concentric layers of the same thickness and whose elastic properties vary according to the distance from the inclusion. In their study, the authors also proposed a method to homogenise the elastic properties of the interface and show that its thickness has little influence on the macroscopic response. On the other hand, it is the fracture properties of the interface which drive the crack path and significantly affect the overall behaviour of the mortar. This influence is explained by the weakness of the interface with respect to the cementitious matrix, which causes the cracks to pass through the inclusion-matrix interface, as shown in Figure 10.

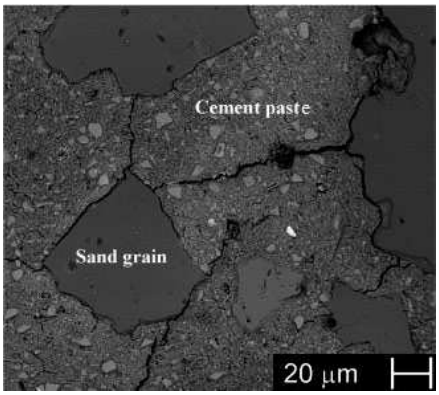

Figure 10. *Cracking at the mortar scale* [60].

In this study, the hydration model is used to simulate the evolution of the hydration near the surface of sand particle. Figure 11 illustrates the evolution of the Young's modulus and the Poisson's ratio within the ITZ, calculated using differential effective medium theory, or D-EMT [19]. The thickness of the ITZ is taken as 20 µm, which the distance above which the elastic moduli no longer change. To calculate the homogenised elastic moduli, the ITZ is subdivided into 10 layers of the same thickness and then homogenised as proposed in [59]. The effective elastic moduli are E_{ITZ} = 14.81GPa and ν_{ITZ} = 0.279. Compared to the bulk cement paste, the difference is explained by the porous nature of the ITZ, leading to a lower Young's modulus and a higher Poisson's ratio. Some authors have observed an important influence of the aggregate shape on the properties of ITZ, particularly the diffusivity and the permeability [61], [62]. However, little to no effect is noticed on the degree of hydration, and little change is witnessed regarding the elastic properties, as long as the sphericity is the particle is close to 1 [61]. The sphericity of the sand used in this study was not measured, but since sand particles in mortar are typically spherical, with sphericity in the range of 0.7-0.95 [63], the exact shape of sand particles was not taken into account. In fact, the integration of complex shapes in the mesostructure generation procedure requires advanced algorithms with additional parameters to calibrate. One of the goals of this study is to provide an upscale methodology that does not depend on additional calibration coefficients at the mesoscale.

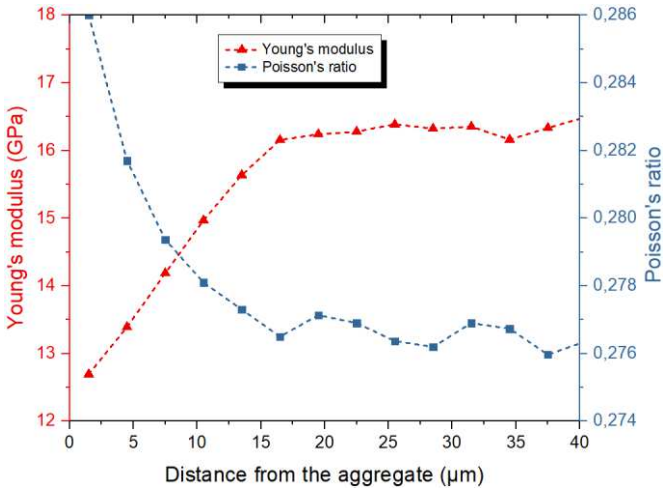

Figure 11. *Evolution of the elastic moduli in the ITZ as a function of the distance from the sand inclusion surface.*

2.4. Grain rupture and particle size effect

Granular materials like sand particles, crushed rocks and gravels are crushable materials and generally have brittle behaviour. The effect of grain size distribution on sand grain crushing has been identified as one of the micromechanisms governing the stress–strain behaviour of sand. McDowell et al. [64], [65] assumed that the phenomenon of particle crushing does not occur spontaneously when a certain stress state is achieved. Instead, it follows the particle size and the survival probabilities of particles which can be described using the Weibull function, from which it follows that the particle size distribution evolves towards a fractal distribution. The effect of particle size on rupture of individual sand and aggregate particles has been studied experimentally [66]–[70] and numerically [71]. Just like with any brittle material, the experimental evidence shows that there is a size effect on the crushing strength, expressed as an inverse relation between particle size and strength.

A study by Jaeger [72] proposed an inversely proportional relationship between the characteristic tensile strength of aggregate particles, σ_f, and the square of the particle size d $(\sigma_f \propto d^{-2})$. Lee [73] proposed a similar empirical relation, where the power coefficient α varies depending on the nature of the sand studied:

$$\sigma_f \propto d^{\alpha} \tag{8}$$

Lee [73] reported values of α equal to -0.357, -0.343 and -0.420 for Leighton Buzzard sand, oolitic limestone and carboniferous limestone, respectively, using grains from d =1 to 50 mm. The effect of grain size on its tensile strength can be written from the empirical law in a probabilistic form using Weibull statistical theory [70]:

$$\sigma_f \propto d^{-n_d/m} \tag{9}$$

where m controls the amplitude of data scatter on crushing strength. Higher m values of around 3 to 4 correspond to sound heterogeneous materials such as quartz sands, biotite and ballast. On the other hand, for feldspars, limestones and carbonates, m varies between 1 and 3. n_d is the geometric similarity of the mechanical problem [74]. For soil particles and rock aggregates under compression and assuming an isotropic homogeneous material, it has

been generally assumed that failure occurs under bulk induced tensile stress, which gives n_d=3 [75]. Ratigan [76] proposed geometric similarities of n_d=2 for tensile failure. However, many results have shown that $n_d \leq 1$ better fits the experimental findings [70], [77].

In this study, the effect of grain size on fracture of sand particles has been applied according to Weibull statistical theory (Equation (9)) where the diameter of sand particles ranges from 1 to 4 mm. n_d and m were taken equal to 1 and 2.85 respectively. It is admitted that the aggregate size distribution has an influence on the damage of concrete [78]–[80], but no study has been found in the literature about the grain size effect on the concrete failure.

3. Numerical results of mortar failure

3.1. A new random particle generation algorithm

Multiple random particle generation methods are proposed in the literature. In general, particles or inclusions of different shapes and orientations are generated and randomly distributed in a given space. A binding matrix is then created in between the inclusions to build the virtual composite material. Among these methods, classical algorithms such as the widely-used take-and-place method [1], [78], [89]–[92], [81]–[88], the random-extension and random-walking algorithms [93]–[95], suffer from a numerical sluggishness due to constant overlap-checking between placed particles during the generation procedure. Alternative methods such as the divide-and-fill [96]–[99] and the heuristic method [100] avoid the overlap-checking, but at the expense of the representativeness of the mesostructure. Such problems occur notably when mesostructures are dense and contain an important number of particles to be placed.

A random particle generation algorithm, designated the zone-of-influence method, is proposed for creating a virtual mesostructure of matrix-inclusion type material systems, e.g. mortar and concrete. This method avoids recursive loops used for overlap-detection as well as complicated rules for placing new particles, thus increasing the effectiveness of the method and its speed. The algorithm can be easily accommodated for different microstructural shapes (notched beams, cylinders, I and H beams, etc.) and works for both 2D and 3D computations. First, particles are subdivided into classes ranging from the biggest to the smallest based on their size, and particles within the same class are considered to have the same size. Second, the REV size and shape are defined. The steps of the placement procedure are the following:

1. For each class C_i, a feasible region $\mathrm{P}_i^{\mathrm{ad}}$ is defined inside the REV (Figure 12-2b). $\mathrm{P}_i^{\mathrm{ad}}$ corresponds to the set of points where the particle can be potentially placed without worrying about overlap. Since no particles have been placed yet, $\mathrm{P}_i^{\mathrm{ad}}$ initially takes account only of the wall effect by removing the edges that correspond to the radius R_i of class C_i.
2. The particles are then placed according to their size starting with the particles of class C_1 (Figure 12-2c). For each new particle with radius R^{N} to be placed, a random position is chosen from $\mathrm{P}_1^{\mathrm{ad}}$ as a definitive position for the particle. The particle is also placed at the same position in all feasible regions of lower sizes (the architecture of the algorithm ensures that if point x exists in P_{α}^{ad}, it also exists in $\mathrm{P}_{\beta,\beta>\alpha}^{ad}$). For each particle in class C_i, a zone of influence $\mathrm{Z}_{\mathrm{inf},i}^{\mathrm{N}}$ is determined according to the equation:

$$\mathrm{Z}_{\mathrm{inf},i}^{\mathrm{N}} = \{x \in \mathrm{P}_i^{\mathrm{ad}}, \|x\| < \mathrm{R}_i + \mathrm{R}^{\mathrm{N}} + \mathrm{G}_i^{\mathrm{N}}\} \qquad \mathrm{i} \in [1, \mathrm{n}] \tag{10}$$

   This zone corresponds to the set of points that would definitely lead to overlap between particles. It is therefore removed from the feasible regions according to size (Figure 12-2c).
3. Once all the particles in C_1 are placed, $\mathrm{P}_1^{\mathrm{ad}}$ is discarded and the algorithm proceeds to the placement of the C_2 particles in the same manner. In the illustrative example, only one

particle from C_1 was placed and only one from C_2 is to be placed. In this case, a random position is chosen from P_2^{ad} without the need for overlap-checking (Figure 12-2d). Since there is only one particle in C_2, there is no need to calculate and remove the zone of influence from P_2^{ad}. This is because no further C_2 particle needs to be placed and therefore no overlap condition needs to be checked with placed C_2 particles (none in this case).

4. P_2^{ad} is then discarded and two particles from C_3 are placed (Figure 12-2e/2f). Here, the first C_3 particle must be placed in P_3^{ad} before including the second particle, otherwise, there is no guarantee that the two particles would not overlap.
5. The procedure continues with the placement of all particles in the last class C_4 by choosing random positions from P_4^{ad} and removing the corresponding zones of influence after each particle placed (Figure 12-2g).
6. Finally, the microstructure is retrieved from the last remaining REV box. As shown in the flowchart of the algorithm presented in Figure 12-1, there is no overlap-checking loop, which considerably reduces the time of the generation method.

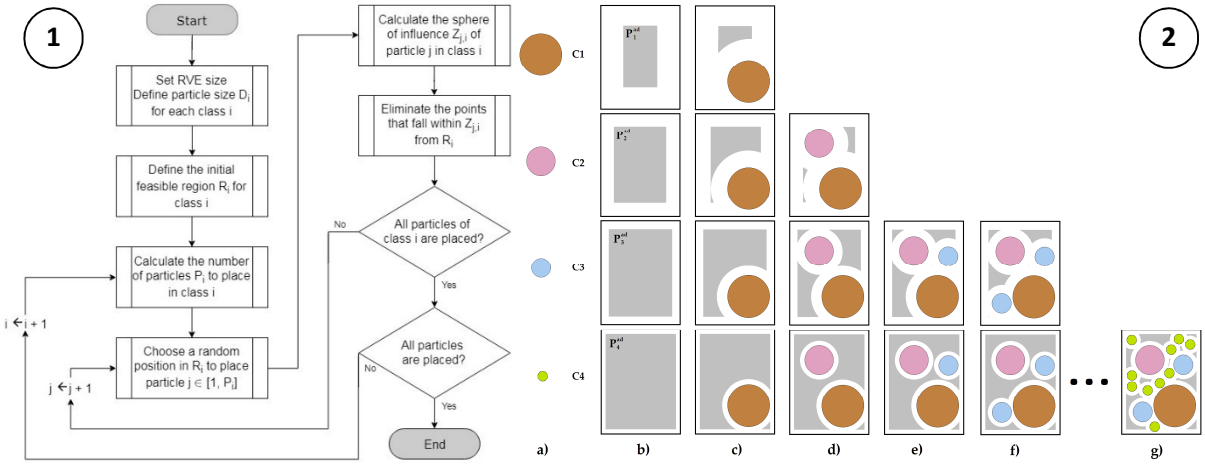

Figure 12. *Zone-of-influence method: (1) algorithm for the random particle generation and placement, and (2) an illustrative step-by-step example for mesostructure generation.*

In order to demonstrate the effectiveness of the new zone-of-influence method (NM) against the old take-and-place method (OM), simulations are carried out by varying the filling degree and the REV size of the mesostructure. The grading curve is subdivided into 9 classes, according to Table 3. Similar conditions are used for both simulations in terms of allocated CPUs and memory. Figure 13-1 shows that, up to a filling degree of 40%, the logarithm of the elapsed time taken by the old method increases linearly with the filling degree, as attested in earlier studies [96]. For higher filling degrees, the elapsed time sharply increases, as the old method struggles to find appropriate places for new particles. In contrast, the time taken by the new method to generate the same mesostructures increases linearly with the filling degree. Using the new method, it is therefore possible to construct a mesostructures with a 55% filling degree in 10 seconds, instead of 30 hours taken by the old method. The new method can also reach higher filling degrees in a short time, e.g. taking only 11 seconds for a filling degree of 73.5%.

On the other hand, Figure 13-2 demonstrates the speed of the new method relative to the classical algorithm. The time it takes to construct the mesostructure with an REV size of 10mm is reduced sixfold by using the new algorithm (~58s with the OM against 9.5s with the NM). The performance increases with REV size, as it takes ~17.1 hours to generate an REV size of 40mm with the OM, but only ~34 minutes with the NM. It was also possible to reach bigger REV sizes with the zone-of-influence algorithm.

Table 3. *Grain size distribution of sand.*

Class	1	2	3	4	5	6	7	8	9
Diameter (mm)	3.6	3.0	2.4	1.8	1.2	0.8	0.6	0.4	0.2
Volume fraction (%)	3.04	3.8	5.51	8.01	16.11	9.11	11.97	15.76	26.68

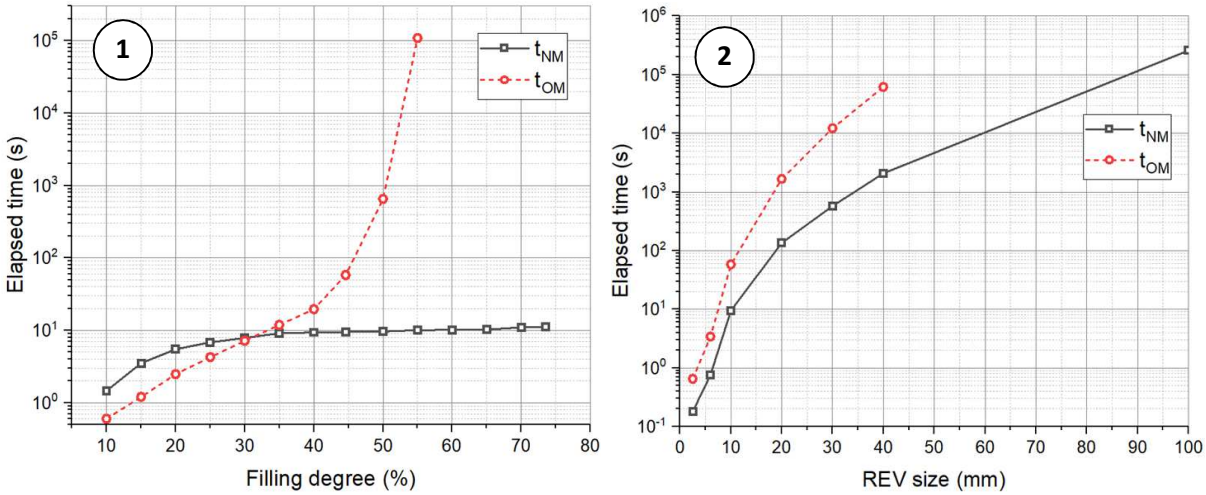

Figure 13. *Comparison between the zone-of-influence (NM) and take-and-place (OM) methods: (1) as a function of the filling degree with a fixed REV size = 10mm, (2) as a function of REV size, with a fixed filling degree = 45%.*

3.2. Mortar beam mesh

The mortar specimen presented in section 2.1 was numerically created using finite elements, by decomposing the beam into three parts, as shown in Figure 14a. To reduce computation time, the two lateral parts (one on each side) were macroscopically represented by a homogenous material whose properties are homogenised mortar. Only the central part, where the damage develops, was represented as a three-phase material, with ITZ modelled by a single homogenised layer. Simulations were performed in 2D plane-stress, by considering a thin thickness of 20mm. This assumption is relevant because we have considered small displacements and at each numerical step they are smaller than the thickness, far from the edge, and the damage does not develop in any finite elements of the lateral parts of the beams. In addition to that, the macroscopic and mesoscopic parts are linked by a connection grid, considered as homogenous material [21], as shown in Figure 14b. Finally, two elastic rods are considered at the bottom of the beam, near the notch, in order to measure the CMOD the same way it was measured experimentally, as illustrated in Figure 14c.

For the mesoscopic part, the new random particle generation method was used to generate the inclusions with their interfaces in the cement paste matrix, respecting the overlap conditions and the boundary limits imposed by the walls and the notch (Figure 14d). The inclusions are approximated by polygons whose number of segments is calculated so as to respect as much as possible a length of 200µm for each segment. In addition, a minimum thickness of cement paste is kept in between inclusions. This choice makes it possible to avoid flocculation of the finite elements corresponding to the inclusions, so as not to create a very rigid mesostructure.

The mesh of the matrix can be created using the '*SURF*' operator proposed in Cast3M. However, for complex geometries such as the cement matrix, this process becomes practically

impossible. In order to avoid computational difficulties of creating fine meshing, a multi-layer contour cutting procedure is used. As illustrated in Figure 15, the cement paste matrix in the mesoscopic part is first segmented into smaller parts, with heights h_1, h_2 ... h_N. The layers are meshed separately and then connected in the final assembly. This procedure makes it possible to create the mesh more quickly (only 6 minutes) without causing problems with regard to the finite element calculations. The average characteristic size of the elements of the binding matrix is about 160µm, which is close to the REV size of cement paste. The initial sand elastic properties have been obtained from an inverse analysis of elastic test on a mortar specimen: E_s = 78GPa, $\nu_s = 0.2$.

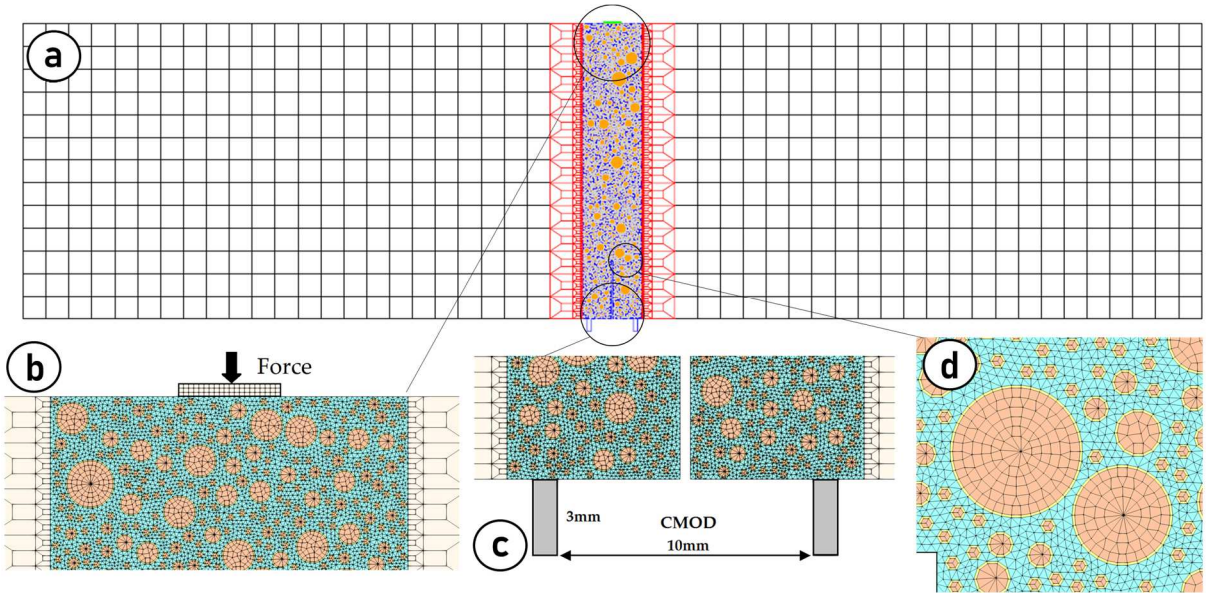

Figure 14. *Mesoscopic finite element construction of mortar beam specimen: a) full specimen with dimensions* $\mathbf{70 \times 70 \times 280mm}$*, b) zoom on the top part of beam, c) zoom on the part of the beam near the notch, d) view of inclusions surrounded by ITZ and binding matrix.*

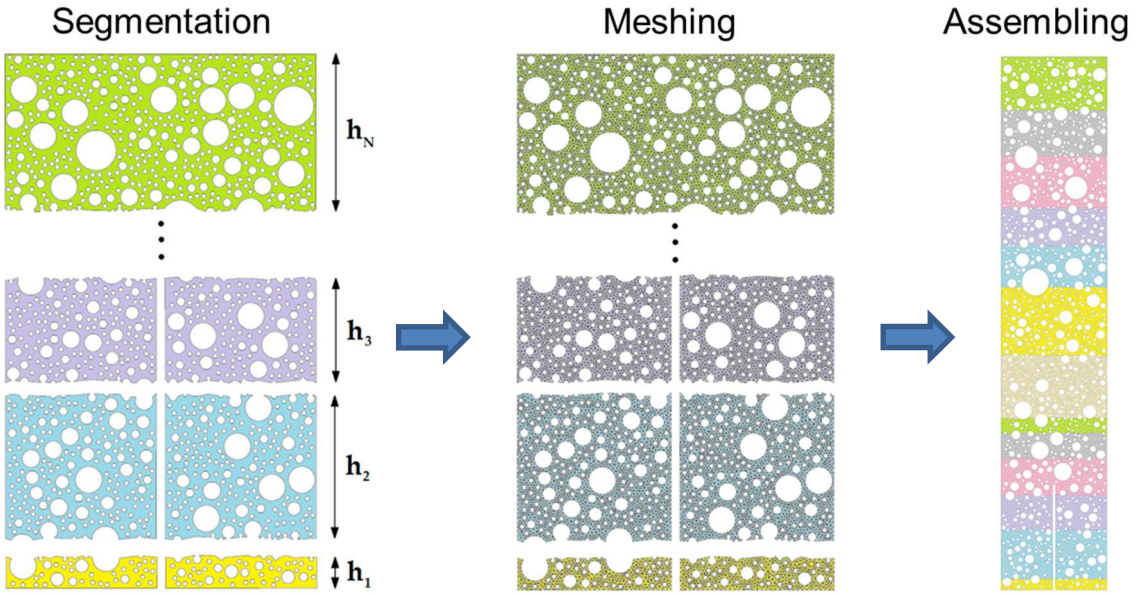

Figure 15. *Three-step procedure of creating the finite element mesh of the cement paste matrix in the mesoscopic part of the beam.*

3.3. Influence of ITZ properties on the mortar damage behaviour

The first series of the simulations (SIM1) do not take into account the presence of the ITZ. The numerical F-CMOD curve is compared to the experimental curve (Figure 16). This comparison shows that the mortar is less resistant and more brittle than expected. An analysis of the crack propagation, shown in Figure 17, reveals that the main crack develops at the tip of the notch and advances inside the bulk matrix with no contribution from the aggregates (no rupture of sand particles). The brittle behaviour observed numerically is therefore attributed to the brittle nature of the bulk cement matrix. Even if a damage behaviour was affected to the sand particles and incorporating the grain size effect (with a variation of the tensile strength from 8 to 15MPa and a variation of the fracture energy from 60 to 120J/m²), no influence was observed on the global response of mortar. These results show the importance of taking into account the ITZ in the simulation of damage in cementitious materials, which was already discussed by many authors [59], [61], [101], [102].

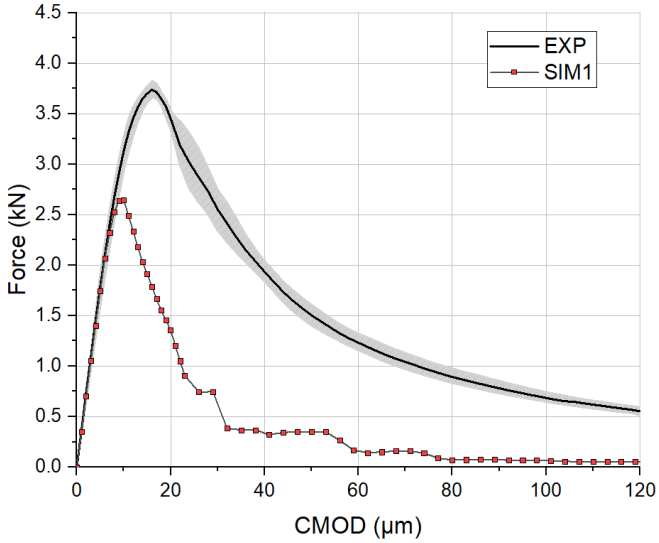

Figure 16. *Force-CMOD curve of the three-point bending test on mortar - absence of ITZ.*

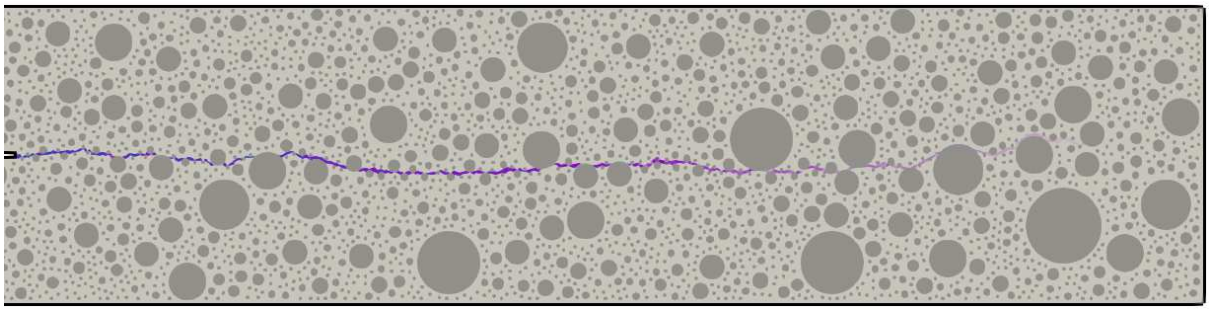

Figure 17. *Crack opening profile in SIM0 simulation - absence of ITZ. (Figure shows only the mesoscopic part).*

The second series of the simulations take into account the explicit representation of the ITZ as a separate phase. The provision of the same fracture properties of the bulk cement paste to the ITZ leads to the same behaviour presented earlier. This means that the ITZ with its distinct properties must be the main contributor to the crack arrest mechanisms. A parametric study was therefore conducted to investigate the influence of such properties. First, the tensile strength was fixed at 6.77MPa (the same as the bulk matrix) and the fracture

energy was varied between 6.8J/m² and 120J/m². The results show that the influence is limited and the numerical Force-CMOD curve is still far from the experimental curve (Figure 18). The crack profile in Figure 19 shows that the increase is driven by the limited contribution of the ITZ's fracture energy when the crack passes along the interface. However, the main crack mostly advances through the bulk cement paste without much interaction from the ITZ. This is explained by the fact that the damage threshold of the ITZ is bigger than that of the bulk paste, since the elastic modulus of the former is smaller due to its porosity (see Equation (4)).

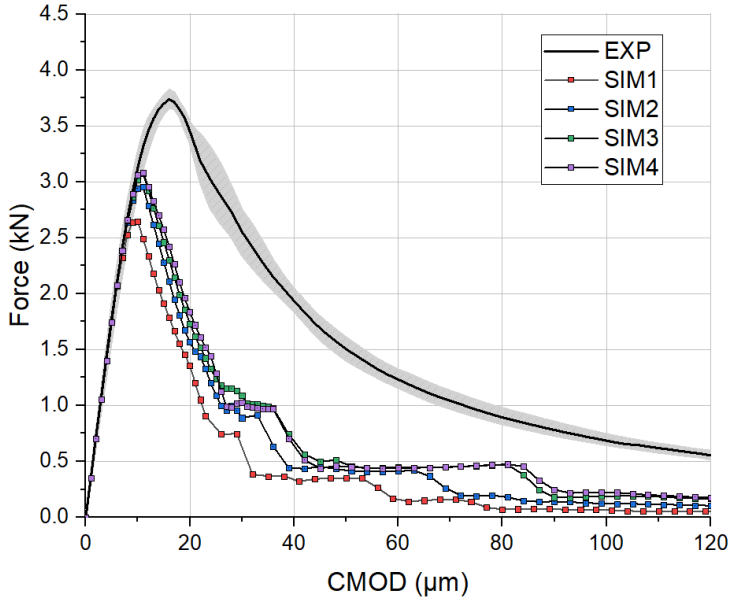

Figure 18. *Influence of the ITZ's fracture energy on the F-CMOD curve ($f_{t,ITZ}$=6.77MPa). SIM2: $G_{f,ITZ}$ = 20J/m², SIM3: $G_{f,ITZ}$ = 50J/m², SIM4: $G_{f,ITZ}$ = 120J/m².*

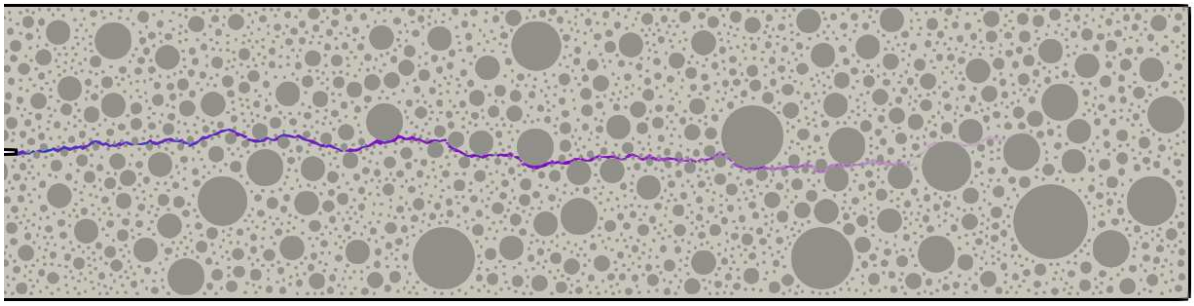

Figure 19. *Crack opening profile in SIM10 simulation – very high fracture energy with the same tensile strength for ITZ as for the cement paste.*

For the third series of the simulations, the tensile strength was reduced to 6MPa in order to decrease the damage threshold of the ITZ. The fracture energy was again varied within the range 20-120 J/m². The resulting F-CMOD curves, shown in Figure 20, show an important variation due to the contribution of the fracture energy of the ITZ to the global ductility of the material. The curves get closer to the experimental curve as the fracture energy increases, but fall short from of the desired behaviour even with high fracture energy for the ITZ (120J/m²).

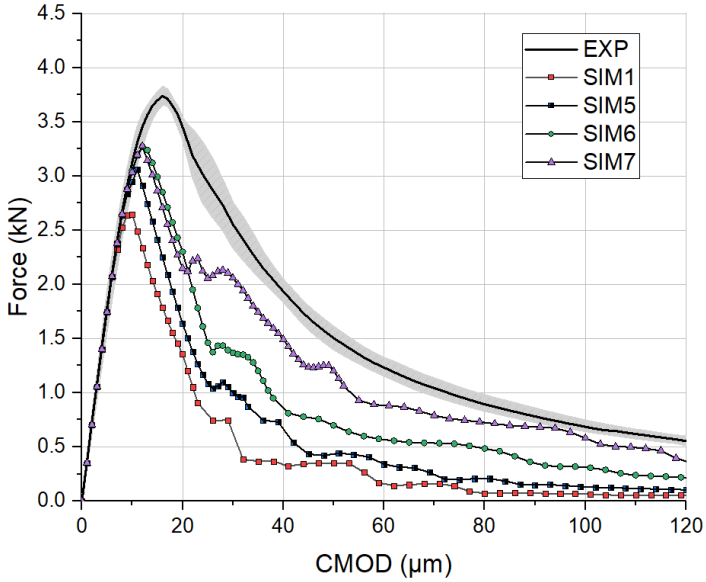

Figure 20. *Influence of the ITZ's fracture energy on the F-CMOD curve ($f_{t,ITZ}$=6MPa). SIM5: $G_{f,ITZ}$ = 20J/m^2, SIM6: $G_{f,ITZ}$ = 50J/m^2, SIM7: $G_{f,ITZ}$ = 120J/m^2*

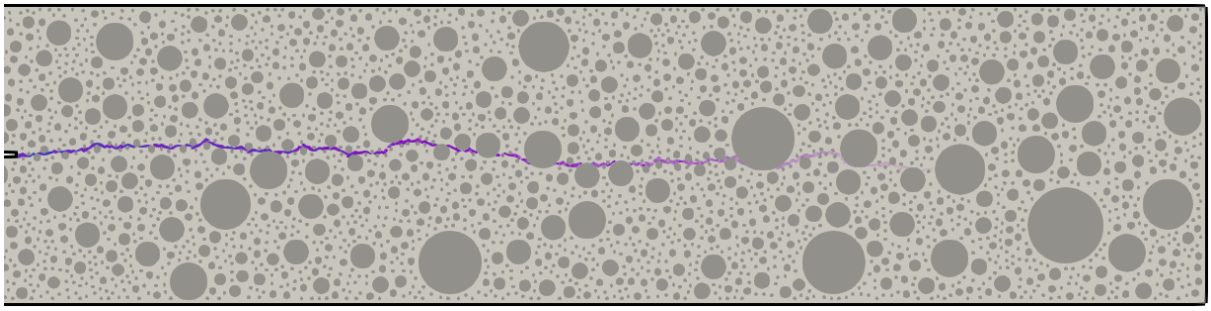

Figure 21. *Crack opening profile in SIM13 simulation – very high fracture energy with a lower tensile strength for the ITZ than for the bulk cement paste.*

3.4. Impact of the sand particle size effect on properties of mortar

The presence of a size effect on individual sand and aggregate particles has been studied for the last series. The properties $f_{t,ITZ}$ = 6MPa and $G_{f,ITZ}$ = 120J/m² were maintained for the ITZ. The grain size effect law was introduced to the fracture behaviour of the sand particles linking the tensile strength to the particle size ranging from 1 to 4mm, according to Equation (9).

The obtained F-CMOD curve, shown in Figure 22, is in good agreement to the experimental behaviour, due to the contributions from the ITZ's absorption of cracks and the fracture of large sand particles which act as crack arrest mechanisms. A close investigation of the damage and the crack opening profiles (Figure 23) shows that the crack advances from the tip of the notch through the bulk and reaches a rather large sand inclusion. Damage grows inside and the main crack passes through the sand particle. The main crack then travels along the ITZ of smaller inclusions which remain unbroken. Damage grows in the surroundings of the main crack. Occasionally, the crack is arrested due to the presence of a large sand particle or the high fracture energy of the ITZ, provoking the bifurcation of the main crack or forcing its deviation through the bulk cement paste.

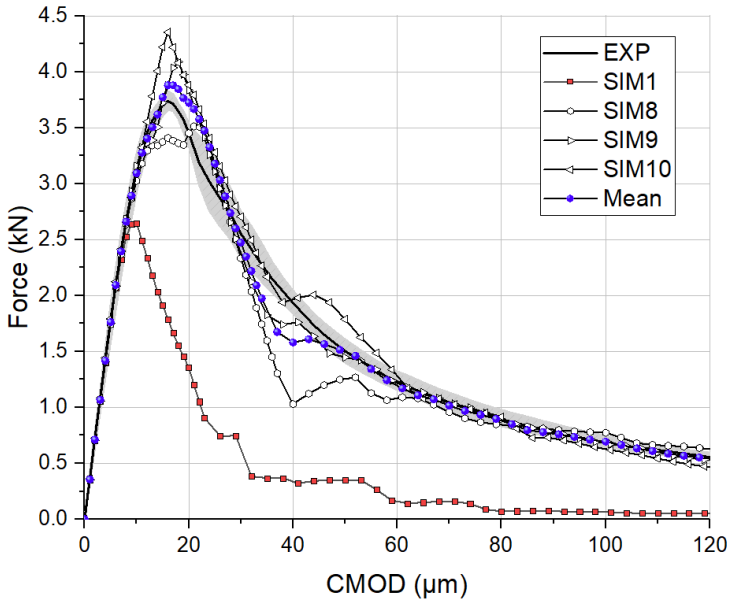

Figure 22. *F-CMOD curve after the attribution of a size effect to the grain fracture.*

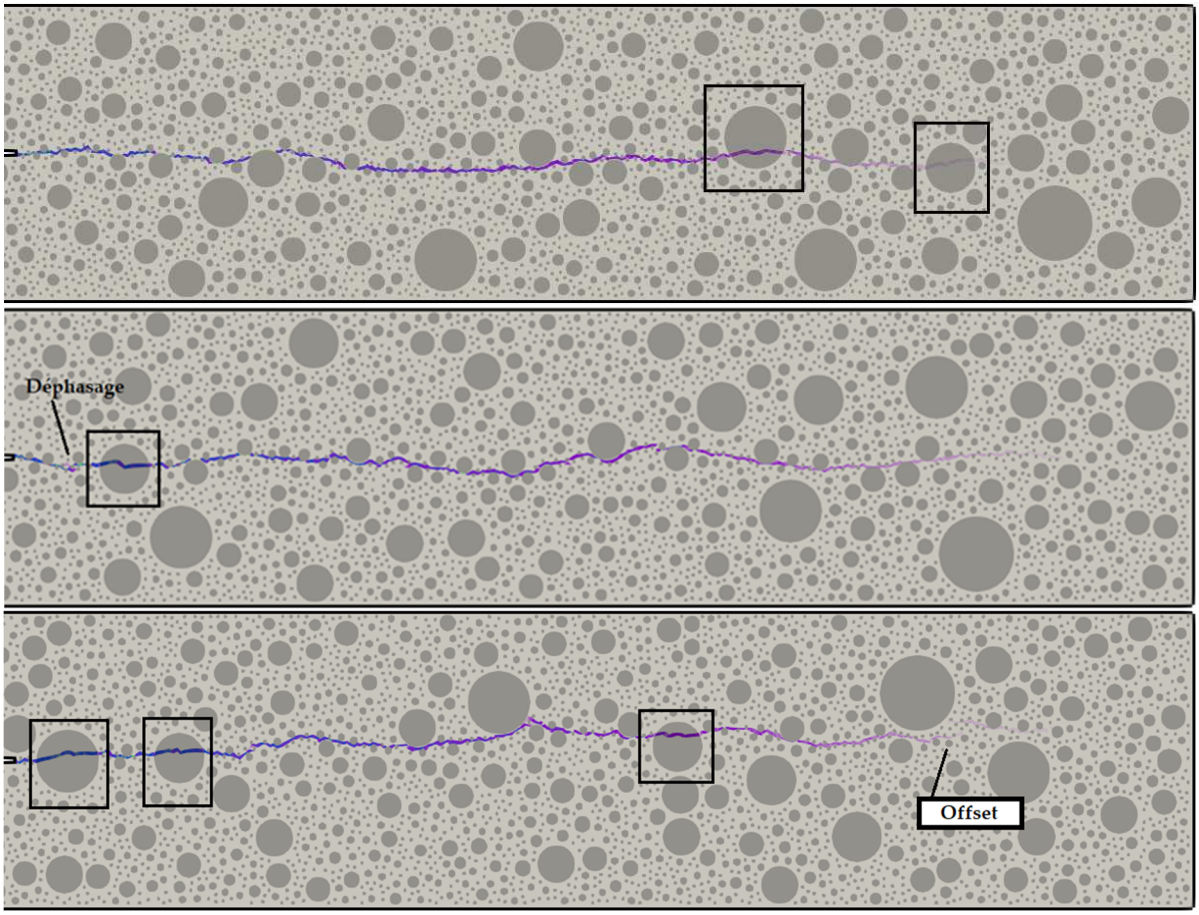

Figure 23. *Crack opening profile of mortar after the attribution of a size effect to the grain fracture (SIM16, SIM17, SIM18) with three different random particle generation.*

Despite obtaining a numerical response for mortar that fits the experimental results and a cracking profile that is characteristic of the material, some questions can be raised relative to the high value found for the fracture energy of the ITZ. While it is true that the presence of more porosity leads to arrest mechanisms and therefore a contribution to the total

fracture energy, test simulations of a porous material with randomly distributed pores under tensile loading show that the total fracture energy can only increase by a small factor (Figure 24). Therefore, the apparent quasi-brittleness of the mortar is unlikely to be explained by the high fracture energy of the ITZ, and more numerical and experimental tests are needed to demonstrate how to fully simulate the damage behaviour of quasi-brittle materials (mortar and concrete) which are composed of a more brittle matrix (cement paste).

This paper does not aim to discuss on the size effect of the structure on the failure of concrete but the above results could be considered in a future work to investigate the influence of the size effect in grains on the size effect of concrete structure. Indeed, recently [79] have showed the influence of the grain-to-structure size ratio on the failure relating to the size effect theory of concrete. It was shown that the inclusion has a significant influence. It will be interesting to analyse the coupling between these two assumptions.

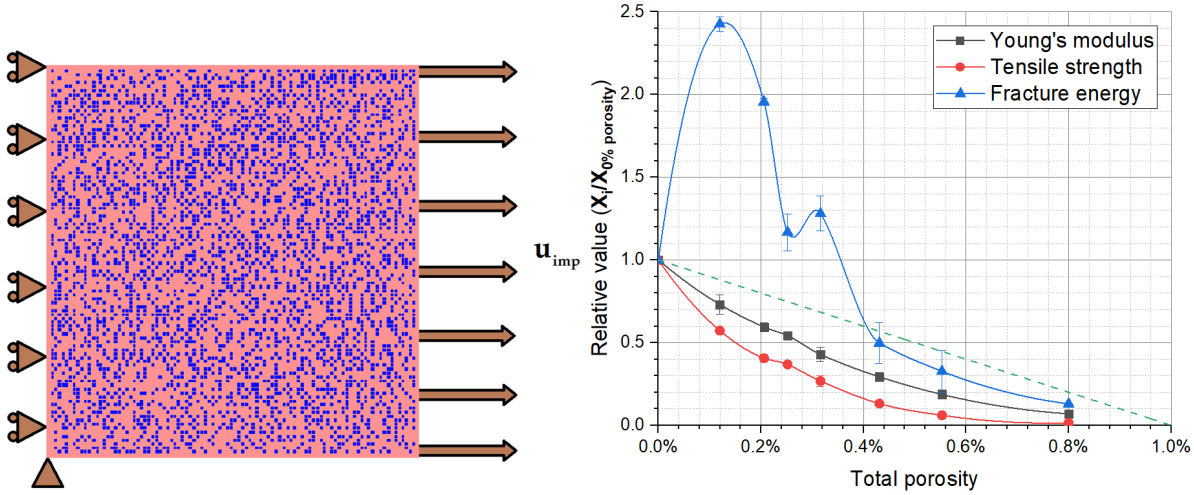

Figure 24. *Evolution of the homogenised fracture properties of a porous microstructure.*

4 Conclusions

The purpose of this article was the development of a descriptive model to characterise the part of each component on the damage behaviour of mortar. For that, a multi-scale approach was suggested starting at the microscopic scale. It was need the determination of the damage properties of the bulk cement paste, that of the interface between the last one and the sand grains, and that of the sand grains.

First of all, the micromechanical properties of cement paste phases were identified and fixed regardless of the cement paste composition. This was achieved by generating a virtual microstructure of a reference cement paste through a hydration model and implementing it in a FE code to simulate the damage behaviour. The homogenised properties of cement paste were identified by comparing to experimental data. Also, this method was used to calculate the properties of the interface between sand grains and the bulk cement paste at the upper scale.

Second of all, a three-point bending test conducted on mortar specimen was simulated using the homogenised properties from the previous scales. A parametric study was conducted with the aim of identifying the influence of the fracture properties of each phase, particularly that of the ITZ and the sand particles. The numerical results show that taking into account the interfacial zone leads to a constitutive behaviour for mortar that is as brittle as that of the bulk cement paste. In addition to that, the simulations also demonstrate the important role of the ITZ properties on the global behaviour of mortar and show that the ITZ must have a smaller tensile strength and higher fracture energy.

The significant result was the highlighting of the size effect of the sand grains on the damage of mortar. It leads to contribute to the change of behaviour of cementitious materials from a brittle nature at the microscopic scale to a quasi-brittle nature in the case of mortar or concrete.

These results are important for the analysis of special concrete mixtures in which there are new materials. For example, the fracture properties of recycled sand grains and recycled aggregates are often discussed because it is difficult to characterise [13], [103]. Also, the influence of fibres in reinforced cementitious materials could be studied using the proposed methodology. In fact, the random particle generation algorithm can be modified in order to account for inclusions with different shapes and orientations, including elliptical particles.

5 Nomenclature

Symbol	Designation	Symbol	Designation
$\{\cdot\}_{\pm}$	Macaulay brackets	$G_{f,ph}$	Fracture energy of the cement phase
α	Sand fracture model parameter	$G_{f,s}$	Fracture energy of the sand particles
α_{ft}	Hardness-tensile strength proportionality constant	G_i^N	Gap between particles of the class C_i when placing new particle with radius R^N (particle generation algorithm)
β_{Gf}	Elastic energy-fracture energy proportionality constant	h	Regulisation length (damage model)
B_T	Model parameter controlling the softening behaviour	HD_{ph}	Hardness of the cement phase
C-S-H	Calcium-silicate-hydrate (cement phase)	*ITZ*	Interfacial transition zone
C_i	Sand particle class i with the same size (particle generation algorithm)	κ_0	Damage threshold
CMOD	Crack mouth opening displacement	m	Sand fracture model parameter
d	Diameter size of sand particle	ν	Poisson's ratio
D_C	Damage due to compressive stress	ν_{HCP}	Poisson's ratio of the hardened cement paste
D_T	Damage due to tensile stress	ν_{ITZ}	Poisson's ratio of the ITZ
DOE	Design of experiments	ν_{ph}	Poisson's ratio of the cement phase
ε_{eq}	Equivalent strain	ν_s	Poisson's ratio of the sand particles
ε_{ii}	Eigenvalues of the strain tensor	n_d	Sand fracture model parameter
E	Young's modulus	*NM*	New method (new particle generation algorithm)
E_{HCP}	Young's modulus of the hardened cement paste	*OM*	Old method (classical take-and-place algorithm)
E_{ITZ}	Young's modulus of the ITZ	P_i^{ad}	Points in the feasible region of class C_i (particle generation algorithm)
E_{ph}	Young's modulus of the cement phase	*REV*	Representative elementary volume
E_s	Young's modulus of the sand particles	R_i	Particle radius of the class C_i (particle generation algorithm)
f_t	Poisson's ratio	R^N	Radius of a new particle to be placed (particle generation algorithm)
$f_{t,HCP}$	Tensile strength of the hardened cement paste	$\boldsymbol{\sigma}$	Total stresses (damage model)
$f_{t,ITZ}$	Tensile strength of the ITZ	$\tilde{\boldsymbol{\sigma}}$	Effective stresses (damage model)
$f_{t,ph}$	Tensile strength of the cement phase	σ_f	Tensile strength of the sand

$f_{t,s}$	Tensile strength of the sand particles	t_{NM}	Time elapsed for the new algorithm of particle generation
FE	Finite element	t_{OM}	Time elapsed for the old algorithm of particle generation
G_f	Fracture energy	$VCCTL$	Virtual Cement and Conrete Testing Laboratory
$G_{f,HCP}$	Fracture energy of the hardened cement paste	w/c	Water-to-cement ratio
$G_{f,ITZ}$	Fracture energy of the ITZ	$Z^N_{inf,i}$	Zone of influence corresponding to the class C_i when placing a new particle with radius R^N (particle generation algorithm)

6 References

[1] Grondin, F., Dumontet, H., Ben Hamida, A., Mounajed, G., and Boussa, H., 2007. Multi-scales modelling for the behaviour of damaged concrete *Cement and Concrete Research* 37:1453–1462.

[2] Grassl, P. and Rempling, R., 2008. A damage-plasticity interface approach to the meso-scale modelling of concrete subjected to cyclic compressive loading *Engineering Fracture Mechanics* 75:4804–4818.

[3] Farah, M., Saliba, J., Grondin, F., and Loukili, A., 2018. Multi-Scale Methods for the Analysis of Creep-Damage Coupling in Concrete *Advances in Multi-Physics and Multi-Scale Couplings in Geo-Environmental Mechanics*:205–241.

[4] Tang, L., Zhou, W., Liu, X., Ma, G., and Chen, M., 2019. Three-dimensional mesoscopic simulation of the dynamic tensile fracture of concrete *Engineering Fracture Mechanics* 211:269–281.

[5] Sherzer, G., Gao, P., Schlangen, E., Ye, G., and Gal, E., 2017. Upscaling Cement Paste Microstructure to Obtain the Fracture, Shear, and Elastic Concrete Mechanical LDPM Parameters. *Materials (Basel, Switzerland)* 10.

[6] Qian, Z., Schlangen, E., Ye, G., and van Breugel, K., 2017. Modeling framework for fracture in multiscale scement-based material structures *Materials* 10.

[7] Mounajed, G., Grondin, F., Dumontet, H., and Ben Hamida, A., 2006. Digital Concrete: A Multi-scale Approach for the Concrete Behavior *Journal of Computational Methods in Sciences and Engineering* 6:325–337.

[8] Bernard, F., Kamali-Bernard, S., and Prince, W., 2008. 3D multi-scale modelling of mechanical behaviour of sound and leached mortar *Cement and Concrete Research* 38:449–458.

[9] Ghabezloo, S., 2010. Association of macroscopic laboratory testing and micromechanics modelling for the evaluation of the poroelastic parameters of a hardened cement paste *Cement and Concrete Research* 40:1197–1210.

[10] Zhang, H., Šavija, B., Chaves Figueiredo, S., Lukovic, M., and Schlangen, E., 2016. Microscale Testing and Modelling of Cement Paste as Basis for Multi-Scale Modelling. *Materials (Basel, Switzerland)* 9.

[11] Contrafatto, L., Cuomo, M., and Gazzo, S., 2016. A concrete homogenisation technique at meso-scale level accounting for damaging behaviour of cement paste and aggregates *Computers & Structures* 173:1–18.

[12] Zhang, H., Šavija, B., Figueiredo, S. C., and Schlangen, E., 2017. Experimentally validated multi-scale modelling scheme of deformation and fracture of cement paste *Cement and Concrete Research* 102:175–186.

[13] Guo, M., Grondin, F., and Loukili, A., 2019. Numerical method to model the creep of

recycled aggregate concrete by considering the old attached mortar *Cement and Concrete Research* 118:14–24.
[14] Fichant, S., La Borderie, C., and Pijaudier-Cabot, G., 1999. Isotropic and anisotropic descriptions of damage in concrete structures *Mechanics of Cohesive-frictional Materials* 4:339–359.
[15] Velez, K., Maximilien, S., Damidot, D., Fantozzi, G., and Sorrentino, F., 2001. Determination by nanoindentation of elastic modulus and hardness of pure constituents of Portland cement clinker *Cement and Concrete Research* 31:555–561.
[16] Luković, M., Schlangen, E., and Ye, G., 2015. Combined experimental and numerical study of fracture behaviour of cement paste at the microlevel *Cement and Concrete Research* 73:123–135.
[17] Němeček, J., Králík, V., Šmilauer, V., Polívka, L., and Jäger, A., 2016. Tensile strength of hydrated cement paste phases assessed by micro-bending tests and nanoindentation *Cement and Concrete Composites* 73:164–173.
[18] Hu, C., Gao, Y., Chen, B., Zhang, Y., and Li, Z., 2016. Estimation of the poroelastic properties of calcium-silicate-hydrate (C-S-H) gel *Materials & Design* 92:107–113.
[19] Bullard, J. W. and Stutzman, P. E., 2006. Analysis of CCRL Portland Cement Proficiency Samples Number 151 and Number 152 Using the Virtual Cement and Concrete Reference Laboratory *Cem. Concr. Res.* 36:1548–1555.
[20] Fichant, S., Pijaudier-Cabot, G., and La Borderie, C., 1997. Continuum damage modelling: Approximation of crack induced anisotropy *Mechanics Research Communications* 24:109–114.
[21] Matallah, M., Farah, M., Grondin, F., Loukili, A., and Rozière, E., 2013. Size-independent fracture energy of concrete at very early ages by inverse analysis *Engineering Fracture Mechanics* 109:1–16.
[22] Pellenq, R. J.-M. *et al.*, 2009. A realistic molecular model of cement hydrates. *Proceedings of the National Academy of Sciences of the United States of America* 106:16102–16107.
[23] Hou, D., Ma, H., Zhu, Y., and Li, Z., 2014. Calcium silicate hydrate from dry to saturated state: Structure, dynamics and mechanical properties *Acta Materialia* 67:81–94.
[24] Hou, D., Zhu, Y., Lu, Y., and Li, Z., 2014. Mechanical properties of calcium silicate hydrate (C–S–H) at nano-scale: A molecular dynamics study *Materials Chemistry and Physics* 146:503–511.
[25] Hajilar, S. and Shafei, B., 2016. Mechanical failure mechanisms of hydrated products of tricalcium aluminate: A reactive molecular dynamics study *Materials & Design* 90:165–176.
[26] Geng, G. *et al.*, 2017. Aluminum-induced dreierketten chain cross-links increase the mechanical properties of nanocrystalline calcium aluminosilicate hydrate *Scientific Reports* 7:44032.
[27] Ye, G., Sun, Z., Voigt, T., van Breugel, K., and Shah, S. P., 2004. A micromechanic model for characterization of cement paste at early age validated with experiments *International RILEM Symposium on Concrete Science and Engineering: A Tribute to Arnon Bentur*:1–11.
[28] Haecker, C.-J. *et al.*, 2005. Modeling the linear elastic properties of Portland cement paste *Cement and Concrete Research* 35:1948–1960.
[29] Bernard, F. and Kamali-Bernard, S., 2010. Performance simulation and quantitative analysis of cement-based materials subjected to leaching *Computational Materials Science* 50:218–226.
[30] Liu, L. *et al.*, 2011. Modeling of the internal damage of saturated cement paste due to

ice crystallization pressure during freezing *Cement and Concrete Composites* 33:562–571.
[31] Ouyang, X., Ye, G., and van Breugel, K., 2017. Experimental and numerical evaluation of mechanical properties of interface between filler and hydration products *Construction and Building Materials* 135:538–549.
[32] Gusev, A. A., 1997. Representative volume element size for elastic composites: A numerical study *Journal of the Mechanics and Physics of Solids* 45:1449–1459.
[33] Bentz, D. P., 1997. Three-Dimensional Computer Simulation of Portland Cement Hydration and Microstructure Development *Journal of the American Ceramic Society* 80:3–21.
[34] Hilloulin, B., Hilloulin, D., Grondin, F., Loukili, A., and De Belie, N., 2016. Mechanical regains due to self-healing in cementitious materials: Experimental measurements and micro-mechanical model *Cement and Concrete Research* 80:21–32.
[35] Verpaux, P., Charras, T., and Millard, A., CASTEM 2000 une approche moderne du calcul des structures, *Calcul des structures et intelligences artificielle, Pluralis*, 1988. [Online]. Available: http://www-cast3m.cea.fr.
[36] Fonseca, P. C., Jennings, H. M., and Andrade, J. E., 2011. A nanoscale numerical model of calcium silicate hydrate *Mechanics of Materials* 43:408–419.
[37] Bernard, O., Ulm, F.-J., and Lemarchand, E., 2003. A multiscale micromechanics-hydration model for the early-age elastic properties of cement-based materials *Cement and Concrete Research* 33:1293–1309.
[38] Qian, Z., Schlangen, E., Ye, G., and Van Breugel, K., 2010. Prediction of mechanical properties of cement paste at microscale *Materiales de Construcción* 60:7–18.
[39] Rhardane, A., Élaboration d'une approche micromécanique pour modéliser l'endommagement des matériaux cimentaires sous fluage et cycles de gel-dégel, Ecole Centrale de Nantes, 2018.
[40] Rhardane, A., Grondin, F., and Alam, S. Y., 2019. Development of a micro-mechanical model for the determination of damage properties of cement pastes *Construction and Building Materials*:(under review).
[41] Zhang, P., Li, S. X., and Zhang, Z. F., 2011. General relationship between strength and hardness *Materials Science and Engineering: A* 529:62–73.
[42] ASTM Standard E 1876 - 01, Standard Test Method for Dynamic Young's Modulus, Shear Modulus, and Poisson's Ratio by Impulse Excitation of Vibration. .
[43] Marquardt, D. W., 1963. An Algorithm for Least-Squares Estimation of Nonlinear Parameters *Journal of the Society for Industrial and Applied Mathematics* 11(2):431–441.
[44] Valentini, L. *et al.*, 2014. Simulation of the hydration kinetics and elastic moduli of cement mortars by microstructural modelling *Cement and Concrete Composites* 52:54–63.
[45] Dolado, J. S. and van Breugel, K., 2011. Recent advances in modeling for cementitious materials *Cement and Concrete Research* 41:711–726.
[46] Mondal, P., Nanomechanical Properties of Cementitious Materials, Northwestern University, 2008.
[47] Anthony, J. W., Bideaux, R. A., Bladh, K. W., and Nichols, M. C., Handbook of Mineralogy, *Mineralogical Society of America*, 2001. [Online]. Available: http://www.handbookofmineralogy.com/.
[48] Howind, T. *et al.*, 2011. Mapping of mechanical properties of cement paste microstructures *Proceedings of 13th International Congress on the Chemistry of Cement*:1–7.
[49] Constantinides, G. and Ulm, F. J., 2004. The effect of two types of C-S-H on the

elasticity of cement-based materials: Results from nanoindentation and micromechanical modeling *Cement and Concrete Research* 34:67–80.
[50] Chen, J., Jin, X., Jin, N., and Tian, Y., 2014. A nano-model for micromechanics-based elasticity prediction of hardened cement paste *Magazine of Concrete Research* 66:1145–1153.
[51] Hlobil, M., Šmilauer, V., and Chanvillard, G., 2016. Micromechanical multiscale fracture model for compressive strength of blended cement pastes *Cement and Concrete Research* 83:188–202.
[52] Hu, C. and Li, Z., 2014. Micromechanical investigation of Portland cement paste *Construction and Building Materials* 71:44–52.
[53] Ralph, J., Mindat Mineral Database, *Hudson Institute of Mineralogy*, 1993. [Online]. Available: https://www.mindat.org/.
[54] Scrivener, K. L., Crumbie, A. K., and Laugesen, P., 2004. The Interfacial Transition Zone (ITZ) Between Cement Paste and Aggregate in Concrete *Interface Science* 12:411–421.
[55] Ramesh, G., Sotelino, E. D., and Chen, W. F., 1996. Effect of transition zone on elastic moduli of concrete materials *Cement and Concrete Research* 26:611–622.
[56] Yang, C. C., 1998. Effect of the Transition Zone on the Elastic Moduli of Mortar *Cement and Concrete Research* 28:727–736.
[57] Lutz, M. P., Monteiro, P. J. ., and Zimmerman, R. W., 1997. Inhomogeneous interfacial transition zone model for the bulk modulus of mortar *Cement and Concrete Research* 27:1113–1122.
[58] Grassl, P., Wong, H. S., and Buenfeld, N. R., 2010. Influence of aggregate size and volume fraction on shrinkage induced micro-cracking of concrete and mortar *Cement and Concrete Research* 40:85–93.
[59] Grondin, F. and Matallah, M., 2014. How to consider the Interfacial Transition Zones in the finite element modelling of concrete? *Cement and Concrete Research* 58:67–75.
[60] Lima, P. R. L., Toledo Filho, R. D., and Melo Filho, J. A., 2013. Compressive stress-strain behaviour of cement mortar-composites reinforced with short sisal fibre *Materials Research* 17:38–46.
[61] Chen, H., Zhu, Z., Lin, J., Xu, W., and Liu, L., Numerical modeling on the influence of particle shape on ITZ's microstructure and macro-properties of cementitious composites: a critical review, *Journal of Sustainable Cement-Based Materials*, 7. Taylor and Francis Ltd., :248–269, 04-Jul-2018.
[62] Xu, W., Ma, H., Ji, S., and Chen, H., 2016. Analytical effective elastic properties of particulate composites with soft interfaces around anisotropic particles *Composites Science and Technology* 129:10–18.
[63] Rorato, R., Arroyo, M., Andò, E., and Gens, A., 2019. Sphericity measures of sand grains *Engineering Geology* 254:43–53.
[64] McDowell, G. R., Bolton, M. D., and Robertson, D., 1996. The fractal crushing of granular materials *Journal of the Mechanics and Physics of Solids* 44:2079–2101.
[65] McDowell, G. R. and Bolton, M. D., 1998. On the micromechanics of crushable aggregates *Géotechnique* 48:667–679.
[66] Dey, T. and Halleck, P., 1981. Some aspects of size-Effect in rock failure *Geophysical Research Letters* 8:691–694.
[67] Bazant, Z. P. and Kazemi, M. T., 1990. Determination of fracture energy, process zone longth and brittleness number from size effect, with application to rock and conerete *International Journal of Fracture* 44:111–131.
[68] Přikryl, R., 2001. Some microstructural aspects of strength variation in rocks *International Journal of Rock Mechanics and Mining Sciences* 38:671–682.

[69] Alonso, E. E., Tapias, M., and Gili, J., 2012. Scale effects in rockfill behaviour *Géotechnique Letters* 2:155–160.
[70] Ovalle, C., Frossard, E., Dano, C., Hu, W., Maiolino, S., and Hicher, P.-Y., 2014. The effect of size on the strength of coarse rock aggregates and large rockfill samples through experimental data *Acta Mechanica* 225:2199–2216.
[71] Norouzi, S., Baghbanan, A., and Khani, A., 2013. Investigation of grain size effects on micro/macro-mechanical properties of intact rock using voronoi element - Discrete element method approach *Particulate Science and Technology* 31:507–514.
[72] Jaeger, J. C., 1967. Failure of rocks under tensile conditions *International Journal of Rock Mechanics and Mining Sciences & Geomechanics Abstracts* 4:219–227.
[73] Lee, D.-M., Angles of friction of granular fills, University of Cambridge, 1992.
[74] Bažant, Z. P. and Planas, J., *Fracture and size effect in concrete and other quasibrittle materials*. CRC Press, 1998.
[75] Lobo-Guerrero, S. and Vallejo, L. E., 2006. Application of Weibull Statistics to the Tensile Strength of Rock Aggregates *Journal of Geotechnical and Geoenvironmental Engineering* 132:786–790.
[76] Ratigan, J. L., Statistical fracture mechanics approach to the strength of brittle rock. Ph.D thesis. 1981.
[77] Hu, W., Dano, C., Hicher, P., Le Touzo, J., Derkx, F., and Merliot, E., 2011. Effect of Sample Size on the Behavior of Granular Materials *Geotechnical Testing Journal* 34:186–197.
[78] Gangnant, A., Saliba, J., La Borderie, C., and Morel, S., 2016. Modeling of the quasibrittle fracture of concrete at meso-scale: Effect of classes of aggregates on global and local behavior *Cement and Concrete Research* 89:35–44.
[79] Alam, S. Y., Zhu, R., and Loukili, A., 2020. A new way to analyse the size effect in quasi-brittle materials by scaling the heterogeneity size *Engineering Fracture Mechanics* 225:106864.
[80] Alam, S. Y. and Loukili, A., 2020. Effect of micro-macro crack interaction on softening behaviour of concrete fracture *International Journal of Solids and Structures* 182–183:34–45.
[81] Wittmann, F. H., Roelfstra, P. E., and Sadouki, H., 1985. Simulation and analysis of composite structures *Materials Science and Engineering* 68:239–248.
[82] Bažant, Z. P., Tabbara, M. R., Kazemi, M. T., and Pijaudier-Cabot, G., 1990. Random Particle Model for Fracture of Aggregate or Fiber Composites *Journal of Engineering Mechanics* 116:1686–1705.
[83] Schlangen, E. and van Mier, J. G. M., 1992. Simple lattice model for numerical simulation of fracture of concrete materials and structures *Materials and Structures* 25:534–542.
[84] Wang, H., Wang, J., and Chen, J., 2014. Micromechanical analysis of asphalt mixture fracture with adhesive and cohesive failure *Engineering Fracture Mechanics* 132:104–119.
[85] Wang, X. F., Yang, Z. J., Yates, J. R., Jivkov, A. P., and Zhang, C., 2015. Monte Carlo simulations of mesoscale fracture modelling of concrete with random aggregates and pores *Construction and Building Materials* 75:35–45.
[86] Wriggers, P. and Moftah, S. O., 2006. Mesoscale models for concrete: Homogenisation and damage behaviour *Finite Elements in Analysis and Design* 42:623–636.
[87] Nguyen, T. D., Apport de la modélisation mésoscopique dans la prédiction des écoulements dans les ouvrages en béton fissuré en conditions d'accident grave, Université de Pau et des Pays de l'Adour, 2010.
[88] Tu, Z. and Lu, Y., 2011. Mesoscale modelling of concrete for static and dynamic

response analysis -Part 1: model development and implementation *Structural Engineering and Mechanics* 37:197–213.
[89] Rodrigues, E. A., Manzoli, O. L., Bitencourt Jr., L. A. G., and Bittencourt, T. N., 2016. 2D mesoscale model for concrete based on the use of interface element with a high aspect ratio *International Journal of Solids and Structures* 94–95:112–124.
[90] Ma, H., Xu, W., and Li, Y., 2016. Random aggregate model for mesoscopic structures and mechanical analysis of fully-graded concrete *Computers & Structures* 177:103–113.
[91] Yaghoobi, A. *et al.*, 2017. Mesoscale Fracture Analysis of Multiphase Cementitious Composites Using Peridynamics *Materials* 10:162.
[92] Traxl, R. and Lackner, R., 2018. Consideration of arbitrary inclusion shapes in the framework of isotropic continuum micromechanics: The replacement Eshelby tensor approach *Mechanics of Materials* 126:126–139.
[93] Du, C., Sun, L., Jiang, S., and Ying, Z., 2013. Numerical Simulation of Aggregate Shapes of Three-Dimensional Concrete and Its Applications *Journal of Aerospace Engineering* 26:515–527.
[94] Zhang, Z., Song, X., Liu, Y., Wu, D., and Song, C., 2017. Three-dimensional mesoscale modelling of concrete composites by using random walking algorithm *Composites Science and Technology* 149:235–245.
[95] Liu, L., Sun, W., Ye, G., Chen, H., and Qian, Z., 2012. Estimation of the ionic diffusivity of virtual cement paste by random walk algorithm *Construction and Building Materials* 28:405–413.
[96] De Schutter, G. and Taerwe, L., 1993. Random particle model for concrete based on Delaunay triangulation *Materials and Structures* 26:67–73.
[97] Caballero, A., López, C. M., and Carol, I., 2006. 3D meso-structural analysis of concrete specimens under uniaxial tension *Computer Methods in Applied Mechanics and Engineering* 195:7182–7195.
[98] Saksala, T., 2018. Numerical modelling of concrete fracture processes under dynamic loading: Meso-mechanical approach based on embedded discontinuity finite elements *Engineering Fracture Mechanics* 201:282–297.
[99] Niknezhad, D., Raghavan, B., Bernard, F., and Kamali-Bernard, S., 2015. Towards a realistic morphological model for the meso-scale mechanical and transport behavior of cementitious composites *Composites Part B: Engineering* 81:72–83.
[100] Song, L., Yu, B., Jiang, Y., and Peng, G., 2016. A stochastic generation method for the two-dimensional geometry modeling of concretes with high contents of star domain aggregates *Applied Mathematical Modelling* 40:8175–8184.
[101] Lavergne, F., Sab, K., Sanahuja, J., Bornert, M., and Toulemonde, C., 2015. Investigation of the effect of aggregates' morphology on concrete creep properties by numerical simulations *Cement and Concrete Research* 71:14–28.
[102] Trawiński, W., Bobiński, J., and Tejchman, J., 2016. Two-dimensional simulations of concrete fracture at aggregate level with cohesive elements based on X-ray μCT images *Engineering Fracture Mechanics* 168:204–226.
[103] Guo, M., Grondin, F., and Loukili, A., 2020. Numerical analysis of the failure of recycled aggregate concrete by considering the random composition of old attached mortar *Journal of Building Engineering* 28:101040.